Contents lists available at ScienceDirect

Applied Catalysis B: Environmental

journal homepage: www.elsevier.com/locate/apcatb

Rational synthesis of silylated Beta zeolites and selective ring opening of 1-methylnaphthalene over the NiW-supported catalysts

Su-Un Lee, You-Jin Lee, Jeong-Rang Kim*, Soon-Yong Jeong

Carbon Resources Institute, Korea Research Institute of Chemical Technology, 141, Gajeong-ro, Yuseong-gu, Daejeon 34114, South Korea

ARTICLE INFO

ABSTRACT

Heavy oil has been by-produced from refinery and petrochemical processes, and its use as low-value fuels has been restricted by stricter environmental regulations due to heavy molecules, multi-ring aromatics, and high sulfur content. In a bi-functional catalyst system of metal and zeolitic acid, balancing metallic (from metal element) and acidic function (from zeolite elements) is essential for harnessing the selective ring opening (SRO) reaction with the aim of upgrading the heavy oil. Here, we report a synthetic strategy to control the acid site distribution of Beta zeolite through the silylation reaction with tetramethyl orthosilicate (TMOS), tetraethyl orthosilicate (TEOS), and tetrabutyl orthosilicate (TBOS) as silylation agents. As the size of alkyl chain group in the silylation agents gets larger, the silylation agents were suppressed to spread into the channels and thus the formation of SiO_2 layer was intentionally occurred on the external surface of the zeolite. Resulting from the selectively deposited SiO_2 layer, NiW metals supported on each silylated Beta zeolite altered the metal distribution and further the balance of metallic and acidic function. NiW catalyst supported on TBOS-silylated Beta zeolite exhibited the best catalytic performance toward the SRO reaction of 1-methylnaphthalene in a fix-bed reaction system, proving the optimal balance of metallic and acidic functions. We expect that this study will benefit the control over the selective silylation reaction in order to optimize the balance of metallic and acidic functions in the bi-functional catalysts, and, hence, to promote properly aromatic saturation (hydrogenation) and ring opening (hydrocracking) for selective ring opening products.

© 2017 Elsevier B.V. All rights reserved.

1. Introduction

Zeolites are crystalline aluminosilicates of various structures containing large active surfaces and ordered micropore network, which accommodate a wide range of industrial applications such as gas adsorption, ion exchange, and separation [1,2]. Especially, the basic structural unit of zeolite frameworks consists of silicon or aluminium atoms tetrahedrally coordinated to four oxygen atoms, but replacing Si^{4+} by Al^{3+} crates a negative charge on the framework [3]. When zeolite framework charges are neutralized by protons, they create acid sites that can facilitate acid-catalyzed reactions, such as isomerization, alkylation, and cracking for hydrocarbons [4,5].

Heavy oil has been by-produced from refinery and petrochemical processes and used as low grade fuel. However, its use has been restricted by stricter environmental regulations due to heavy molecules, multi-ring aromatics, and high sulfur content in the heavy oil. Due to the regulations and persistent high oil prices,

upgrading process of heavy oil to high-value middle distillates with low aromatics has attracted interest to many researchers. In the requirements of improving environmental protection and the low-value heavy oil, the acid sites of zeolites have been widely applied for converting the heavy oil to high-value lighter products [6]. More interestingly, multi-ring aromatics, the major components of the heavy oil, can be converted through the selective aromatics ring opening (SRO) reaction into lighter aromatics including benzene, toluene, ethyl-benzene, and xylene (BTEX) [7]. However, for high yield toward desirable mono-ring aromatics, aromatic saturation (hydrogenation) and ring opening (hydrocracking) should be properly proceeded to maintain mono-ring aromatics and avoid the loss into excessive cracked fractions [7,8].

By introducing metal elements into zeolites, not only acidic function from zeolites but also metallic function from metal elements can promote ring opening and aromatic saturation step, respectively, as bi-functional catalytic system [8–10]. To fully exploit the advantages of bi-functional catalytic system, balancing the functions of metal and zeolites is critical in the way of controlling the ratio of metal to acid sites [11–13] and the proximity between both sites [14–17]. In particular, the acid sites on zeolites

can influence the catalytic conversion and selectivity depending on being located on the external surface or channels [2,3]. Furthermore, the different metal-support interaction induced by being deposited on these acid sites can alter the electronic properties of metal [18]. Taken together, once the correlation of the catalytic activities according to the distribution of the acid sites and their metal-zeolite interaction is clarified, it will pave an alternative way to give fine control over the bi-functional catalyst system. However, due to the complexity of maneuvering the acid site distribution of the zeolite, the realization of such bi-functional catalysts has been rarely reported.

Generally, common post-synthetic methods to control the acid sites are cation exchange and dealumination [19]. Cation exchange decreases Brønsted acidity and leaves Lewis acid sites intact. Alternatively, dealumination (i.e., in HCl) removes framework Al cations and leaves behind SiOH as vacancies, decreasing Lewis and Brønsted sites. Although both post-synthetic methods are well established, selectively tuning the distribution of the acid sites has been limited. One feasible method is the formation of mild Brønsted sites via silylation reaction onto hydroxyl groups on the surface of zeolite, which form Si—O—Si or Si—O—Al bonds to lose sufficient strength to crack as the original acid sites [20]. With adopting the silylation agents in larger molecular size than the pore opening of the zeolites, the silylation agents are hindered to diffuse into the pores, so the deposition of SiO_2 layer can be intentionally conducted on the external surface [21]. In this respect, the silylation reaction can enable to investigate the function of acid sites in channels, apart from in the external surface.

Herein, we report a novel synthetic strategy to modify the distribution of acid sites on the external surface and channels in zeolites. As for a bi-functional catalysts targeting the SRO reaction, Beta zeolite with SiO_2/Al_2O_3 molar ratio of 38 (denoted as Beta(38)) was chosen because of the sufficient pore opening of 5.7×7.5 Å to diffuse the bulky of multi-aromatics [22]. Based on the silylation reaction, the distribution of the acid sites on the zeolites was modified by varying the alkyl chain of the silylation agents as tetramethyl orthosilicate (TMOS), tetraethyl orthosilicate (TEOS) and tetrabutyl orthosilicate (TBOS). The silylation agents with the different alkyl chain were employed due to our expectation that the SiO_2 layer can be selectively overcoated to the external surface or channels in accordance with the molecular size of their silylation agents. To investigate the relationship with the distribution of acid sites and catalytic performance of the bi-functional catalysts, NiW catalysts supported on three types of silylated Beta(38) were applied for the SRO reaction of 1-methyl naphthalene (1-mNap) as a model reaction of multi-ring aromatics. The present study can give a rational guideline for the modification of zeolite acid sites with proper silylation agents, and will contribute to devise the efficient bi-functional catalysts.

2. Experimental section

2.1. Catalyst preparation

2.1.1. Silylated-Beta(38)

Silylated-Beta(38) zeolite materials were prepared by following the literature with some modifications [20]. Commercial Beta zeolite (CP814C, SiO_2/Al_2O_3 mole ratio = 38) purchased from Zeolyst Co. was calcined in air atmosphere at 550 °C for 5 h in order to remove impurities and obtain the hydrogen-form zeolite from the ammonium-form. The zeolite (2 g) was mixed with a 50.0 ml of hexane in a three-neck equipped with a reflux condense, and then the solution was heated to 70 °C under moderate stirring. When the solution was maintained at 70 °C, silylation agents corresponding to a loading of 4.0 wt% SiO_2 was injected into the mixture. Depend-

ing on the alky chain of the silylation agents, 0.2 ml of tetramethyl orthosilicate (TMOS), 0.3 ml of tetraethyl orthosilicate (TEOS) or 0.489 ml of tetrabuthyl orthosilicate (TBOS) was added, respectively. After the mixture was kept for 1 h, hexane was removed from the resulting solution by aspiration. The samples were dried at 120 °C for 12 h and calcined in air atmosphere at 500 °C for 4 h. Three types of silylated Beta(38) zeolite were denoted as TMOS-, TEOS-, and TBOS-silylated Beta(38), and compared with Beta(38) zeolite untreated by the silylation.

2.1.2. NiW/silylated-Beta(38) and NiW/Beta(38)

As bi-functional catalysts, NiW/silylated-Beta(38) and NiW/Beta(38) were prepared by a co-impregnation method with an aqueous solution of the appropriate amounts of nickel (II) nitrate hexahydrate $(Ni(NO_3)_2 \cdot 6H_2O$, 98%, purchased from Samchun) and ammonium metatungstate hydrate $((NH_4)_6H_2W_{12}O_{40} \cdot xH_2O$, 66.5 wt%, purchased from Sigma-Aldrich). The 1.1 mmol of Ni and 1.1 mmol of W per 1 g of zeolite were loaded onto as-prepared Beta(38), TMOS-silylated Beta(38), TEOS-silylated Beta(38) and TBOS-silylated Beta(38), respectively. After the impregnation step, the water solvent was removed under vacuum in a rotary evaporator. The collected powder sample was dried at 120 °C in an oven for 12 h, and followed by calcination in an air atmosphere at 550 °C for 4 h.

2.1.3. NiW/Silica(Q-3)

Commercial amorphous silica (Q-3, average pore diameter = 3 nm) purchased from Fusi silysia chemical LTD. was calcined in air atmosphere at 550 °C for 5 h in order to remove impurities. NiW/Silica(Q-3) was prepared as the same procedure for NiW/Beta(38) and NiW/silylated Beta(38). The 1.1 mmol of Ni and 1.1 mmol of W per 1 g of silica (Q-3) were loaded onto as-prepared Silica(Q-3), and then the water solvent was removed under vacuum in a rotary evaporator. The collected powder sample was dried at 120 °C in an oven for 12 h, and followed by calcination in an air atmosphere at 550 °C for 4 h.

2.2. Catalyst characterization

Wide angle powder X-ray diffraction (XRD) patterns were obtained with a Rigaku Ultima IV Diffractometer (40 kV, 40 mA, Cu-Kα radiation) in the 2θ range of 5–80° using a PDXL program. Transmission electron microscopy (TEM) images and TEM-energy-dispersive X-ray spectroscopy (TEM-EDS) elemental analysis were taken using a field emission gun transmission and scanning transmission electron microscope (FEG-S/TEM, FEI-Talos F200S) operating at 200 kV. The bulk elemental composition was determined by inductively-coupled plasma-atomic emission spectrometer (ICP-AES, SHIMADZU ICPS-1000IV) after the dissolution of the sample in the mixture of HF and H_2NO_3, in which the enrichment of Si was observed in consideration of conventional Beta(38) zeolite known as Si/Al = 19. To measure N_2 adsorption/desorption isotherms, the sample was degassed under vacuum at 200 °C for 6 h and N_2 adsorption/desorption was carried out at −196 °C by using a Micromeritics ASAP2020 instrument. The total surface area was calculated by the BET equation, and the pore volume was measured from the total N_2 adsorption amount. The temperature programming desorption of ammonia (NH_3-TPD) was carried out for acidity measurement using BELCAT-B equipped with a thermal conductivity detector (TCD). The sample was pretreated in a H_2 (5%)/Ar flow at 400 °C for 100 min, then cooled down to 100 °C under a He flow. The sample was exposed to a NH_3 (30 mol%)/He flow for 30 min, followed by purging in the He flow for 90 min for elimination of weakly physisorbed ammonia. The sample was heated in the He flow from 100 °C to 500 °C at a heating rate of 10 °C/min and the amount of the desorbed ammonia was detected by TCD.

The temperature programming reduction (TPR) was carried using BELCAT-B equipped with a thermal conductivity detector (TCD). The sample was outgassed by heating at 10 °C/min in a He flow up to 200 °C and equilibrating at 200 °C for 1 h. Then, it was cooled down to 40 °C, and the He flow was converted to a 5% H_2/Ar flow and kept at 40 °C for 3 h. When the TCD signal was stabilized, the temperature and TCD signals were taken by heating the reactor up to 1000 °C at a constant rate of 10 °C/min. The water product was trapped by passing the effluent gas from the reactor through a trap of molecular sieves 13X. X-ray photoelectron spectroscopy (XPS) measurements were carried out using a KRATOS AXIS NOVA spectrometer with monochromatic Al Kα X-ray (1486.6 eV) as the light source. XPS data were calibrated using the C 1 s peak at 284.5 eV. Thermal gravimetric analysis (TGA) was carried out for the coke amount in the spent catalyst after the reaction test. Each spent catalyst was collected by centrifugation and washing with acetone after the reaction. Prior to each TGA, the sample was pretreated by heating at 10 °C/min in a N_2 flow up to 200 °C and equilibrating at 200 °C for 0.5 h. Then, the sample were evaluated in an air atmosphere, ramped up from 50 °C to 1000 °C by 10 °C/min.

2.3. Catalytic performance tests

The SRO of 1-mNap were carried out at 400 °C and 50 barg using a fix-bed reaction system. Before testing the catalytic performance, the catalyst was sulfidated in a tubular furnace by a H_2S (10 mol%)/H_2 flow at 350 °C for 3 h. 1 g of the sulfidated catalyst was loaded in the reactor, followed by leak test. The catalyst was pretreated with a H_2 flow at 400 °C under atmospheric pressure for 8 h to reduce metal components. Then, the pressure increased to 50 barg, and the liquid feed of 1-mNap was delivered at flow rate of 0.037 cm^3/min using a liquid pump along with the H_2 flow of 175 SCCM (H_2/1-mNap mol ratio = 30). The reaction product was cooled down to 5 °C and the liquid product was collected every 2 or 3 h. Gas yield was calculated from the weight of the liquid product. The liquid product was identified by gas chromatography coupled with mass spectrometry (GC–MS, Agilent 7890A/5975C) for qualitative analysis and a frame ionization detector (GC-FID, Younglin 6100) for quantitative analysis. Both of them were equipped with DB-5MS UI capillary column.

3. Result and discussion

3.1. Morphological and physical properties of silylated Beta zeolites

In a typical synthesis for the silylation of Beta(38) zeolite, we employed TMOS, TEOS, and TBOS as silylation agents to site-selectively proceed the silylation reaction by varying the alkyl chain, and three types of silylated Beta(38) were denoted as TMOS-, TEOS-, and TBOS-silylated Beta(38). In Fig. 1, the powder X-ray diffraction (XRD) patterns of the silylated Beta(38) zeolites demonstrated the characteristic diffraction peaks associated with a highly crystalline zeolite BEA framework. Compared to the untreated Beta(38) zeolite, a discernable change in peak intensity and position was not observed, so it proves that the crystal structure of the untreated Beta zeolite is still preserved even after the silylation and the silylated SiO_2 has an amorphous phase or the small particle size below the detection limit of this technique. However, the bulk Si/Al atomic ratio analyzed by inductively-coupled plasma-atomic emission spectrometer (ICP-AES) was significantly increased by the silylation, clearly indicating the SiO_2 formation after the silylation as described in Table 1.

Furthermore, in Fig. 2, representative transmission electron microscopy (TEM) images of the products clarified the effect of
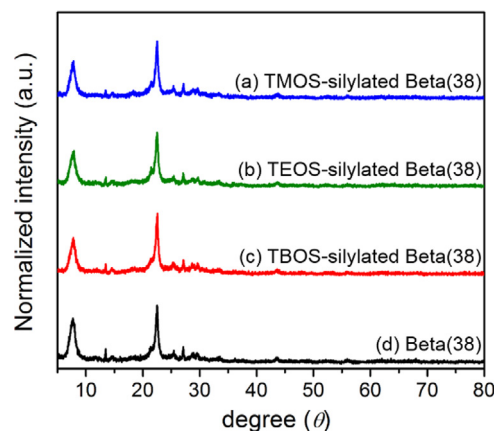

Fig. 1. XRD patterns of (a) TMOS-, (b) TEOS-, (c) TBOS-silylated Beta(38), and (d) Beta(38).

Table 1
Bulk Si/Al atomic ratios of silylated Beta(38) and Beta(38) determined by ICP-AES analysis.

Bulk Si/Al atomic ratio	TMOS-silylated Beta(38)	TEOS-silylated Beta(38)	TBOS-silylated Beta(38)	Beta(38)
ICP-AES	24.6	25.2	24.2	22.8

Table 2
EDS- and XPS-determined Si/Al atomic ratios of silylated Beta(38) and Beta(38).

Si/Al atomic ratio	Entire region EDS (unit area)	Surface XPS
TMOS-silylated Beta(38)	20.8	19.9
TEOS-silylated Beta(38)	19.9	21.7
TBOS-silylated Beta(38)	19.0	21.6
Beta(38)	18.6	19.6

the silylation on the external surface of Beta(38) zeolite. While Beta(38) zeolite has a clear crystalline plane with a stepped surface, three types of the ilylated Beta(38) have demonstrated the amorphous phase, which is a typical characteristic phase of SiO_2 [19], in agreement with the XRD results. From this finding, the external surface of zeolite can be modified as being covered with a SiO_2 layer, irrespective of the silylation agents.

To verify the distribution of the SiO_2 deposition depending on the different silylation agents, the Si/Al atomic ratios were measured by elemental spectroscopic analysis using energy-dispersive X-ray spectroscopy (EDS) and X-ray photoelectron spectroscopy (XPS) analysis in Table 2. In general, for the entire region, EDS-determined Si/Al atomic ratio [23–25] reflect the entire region per unit area (or the bulk composition of several micron range). The unit area of each sample analyzed by EDS measurement was marked as a red square in Fig. S1 in the supporting information. For the surface analysis, the XPS-determined Si/Al atomic ratio reflects the surface composition below analysis depths of about 2–10 nm [26–28]. Since the silylation reaction fundamentally accompanied the coverage of the external surface with the SiO_2 layer as revealed above, all Si/Al atomic ratios of the silylated Beta(38) increased in comparison to that of Beta(38) zeolite. When it comes to the least increment of EDS-determined Si/Al atomic ratio (bulk composition) for the TBOS-silylated Beta(38) zeolite, it may be attributed that large alkyl chain groups suppress hydrolysis due to the steric hindrance, so the degree of silylation decreased according to alkyl chain group used for silylation agents [29]. On the other hand, TBOS-silylated Beta(38) has the highest surface Si/Al atomic ratio based on XPS analysis, despite the least Si/Al atomic ratio of the entire region
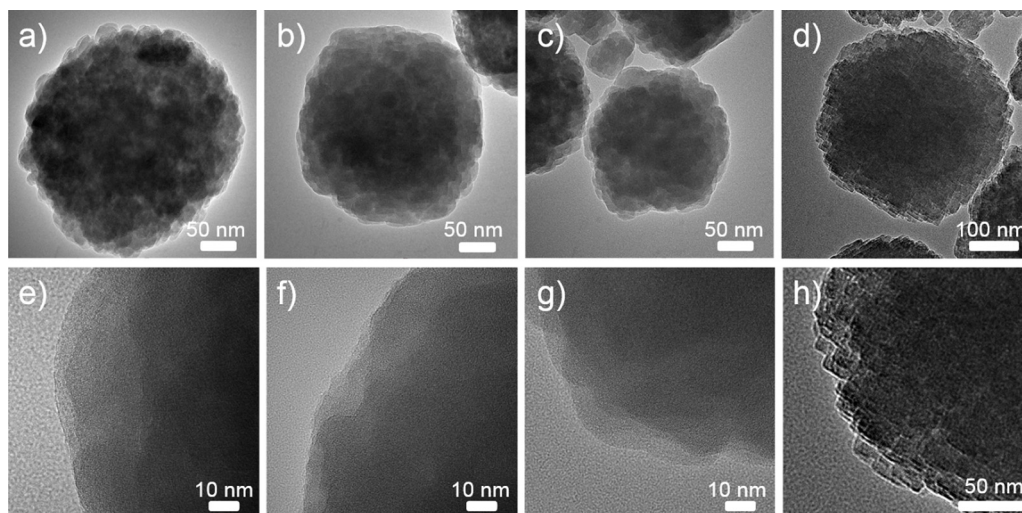
Fig. 2. Representative TEM images (a-d) and magnified TEM images on the surface (e-h); (a, e) TMOS-, (b, f) TEOS-, (c, g) TBOS-silylated Beta(38), and (d, h) Beta(38).

from EDS analysis. Although these ratios cannot be compared as an absolute figure because of different technical analyzing method, it can be assumed that the SiO$_2$ deposition is relatively favored on the surface as the increment of XPS-determined Si/Al atomic ratio is higher than the increment of EDS-determined Si/Al atomic in comparison with that of Beta(38) zeolite. In this sense, it implies that the formation of SiO$_2$ layer was gradually concentrated on the external surface of the zeolite in the order of TMOS-, TEOS-, and TBOS-silylated Beta(38). Based on these findings, the silylation agents with larger alkyl chain groups lead to the formation of SiO$_2$ layer preferentially on the external surface, rather than spreading into the channels.

The influence of the silylation on physical properties was identified by the N$_2$ adsorption analysis with BET method. Surface area and pore volume of the silylated Beta(38) and Beta(38) zeolite are summarized in Table S1. As a result of the silylation, the deposition of the SiO$_2$ layer has produced a small reduction in the surface area. Among them, TBOS-silylated Beta(38) has shown the least decrease in the surface area, which may be related to the low silylation reactivity as following larger alkyl chain groups of the silylation agents. Interestingly, pore volume meagerly decreased, and thus it can be expected that this modification does not significantly impede the diffusion of reactants for their catalytic performance.

3.2. Morphological and physical properties of NiW/silylated Beta catalysts

For the bi-functional catalysts, 1.1 mmol of Ni and 1.1 mmol of W per 1 g of the zeolites were loaded onto as-prepared silylated Beta(38) by the wet impregnation method, and denoted as NiW/silylated Beta(38). N$_2$ adsorption analysis (Table S2) exhibited that the surface area and pore volume significantly decreased due to being covered with Ni and W species [30]. More clearly, representative TEM images of NiW-supported zeolites in Fig. 3 reveal that the NiW nanoparticles were gradually concentrated on the outer part of silylated Beta(38) in the order of NiW/Beta(38) $\approx$ NiW/TMOS-silylated Beta(38) < NiW/TEOS-silylated Beta(38) < NiW/TBOS-silylated Beta(38). It may be explained that the SiO$_2$ layer deposited on the external surface, due to the larger silylation agents, would shrink the pore opening and thus intervene the loading of Ni and W into the inner channels of silylated zeolites.

According to the XRD patterns in Fig. 4, the characteristic diffraction peak positions of the NiW/silylated Beta(38) and NiW/Beta(38)
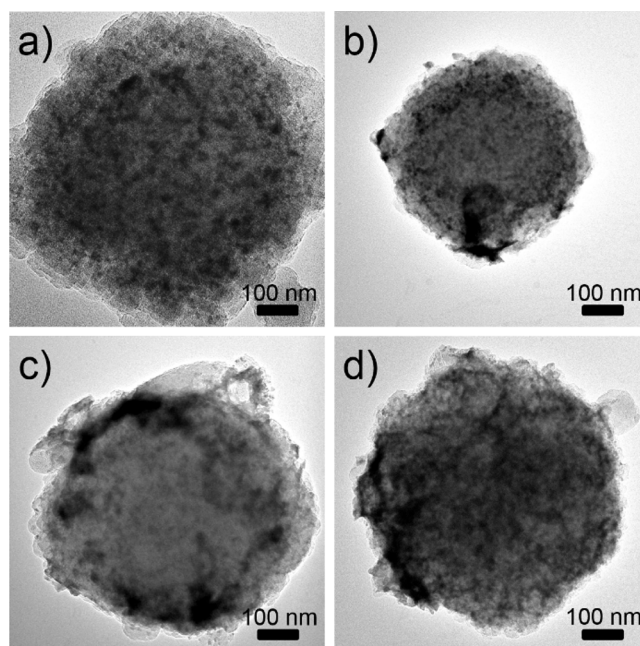

Fig. 3. TEM images of (a) NiW/TMOS-, (b) NiW/TEOS-, (c) NiW/TBOS-silylated Beta(38), and (d) NiW/Beta(38).

were remained unchanged compared to that of Beta(38), proving the maintenance of Beta zeolite crystal structure. However, the weakened peak intensity means that impregnated metal species resulted in the dilution effect or partial breakdown of zeolite structure [31]. Notably, additional peaks were observed, indicating part of tungsten and nickel oxidized species such as WO$_3$ or Ni$_2$O$_3$ in amorphous phase or microcrystalline [32–34], which might be the NiW particles confirmed by the above TEM images.

3.3. Electronic properties of NiW/silylated Beta catalysts

To further investigate the oxidation states of the impregnated metal species, XPS analysis was demonstrated in Fig. 5. In the W 4f spectra of all samples, spin-orbit split lines of W 4f$_{5/2}$ and 4f$_{7/2}$ electrons were appeared at binding energy positions of 37.8–38.3 and 35.7–36.3 eV [35]. Theses peaks are assigned to W^{6+}, most likely to be WO$_3$. In the meantime, the peak positions of W sup-
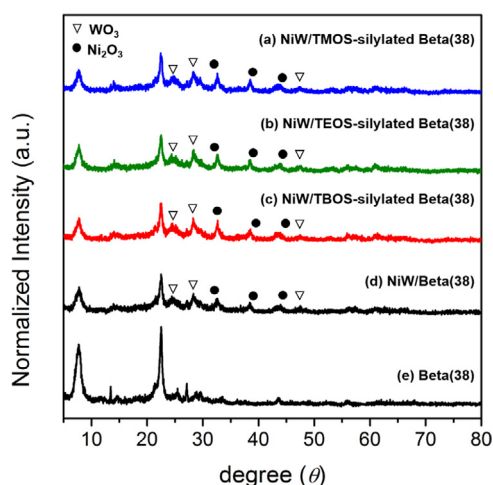
Fig. 4. XRD patterns of (a) NiW/TMOS-, (b) NiW/TEOS-, (c) NiW/TBOS-silylated Beta(38), (d) NiW/Beta(38), and (e) Beta(38). The position of WO_3 and Ni_2O_3 references were taken from the JCPDS database (WO_3: 85-2460, Ni_2O_3: 14-0481).

ported on silylated Beta(38) were slightly shifted towards lower BE values as compared with those supported on untreated Beta(38), reflecting more reduced states. It suggests that the surface modification of zeolites by the silylation strengthen the interaction of W with the supporting zeolites [35]. In the Ni 2p spectra of all samples, spin-orbit split lines of Ni $2P_{3/2}$ and $2p_{1/2}$ were located at 856.2–856.5 and 873.8–874.3 eV. These Ni species can be correlated with Ni^{3+}, such as Ni_2O_3 [33,35], under the coexistence with oxidized W phase. However, the peak positions of Ni supported on the different silylated Beta(38) remained the same as those supported on untreated Beta(38) zeolite.

By means of H_2-temperature programming reduction (H_2-TPR) measurement, the interaction between metal oxide species and supports was further verified in Fig. 6. The TPR profiles presented three peaks of hydrogen consumption between 600 and 800 °C. The low-temperature peak around 630 °C can be regarded as the reduction of octahedrally coordinated polymeric W species and mostly Ni oxidic species, and the high-temperature peaks over 700 °C can be assigned to the reduction of tetrahedrally coordinated or dimeric W species [31,36]. While the low-temperature peak of NiW/silylated Beta(38) shifted to the lower temperature, the high temperature peaks shifted to the higher temperature in comparison with NiW/Beta(38). Furthermore, total H_2 consumption in NiW/silylated Beta(38) increased more than NiW/Beta(38).
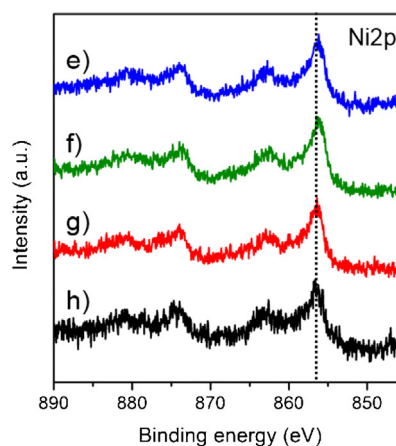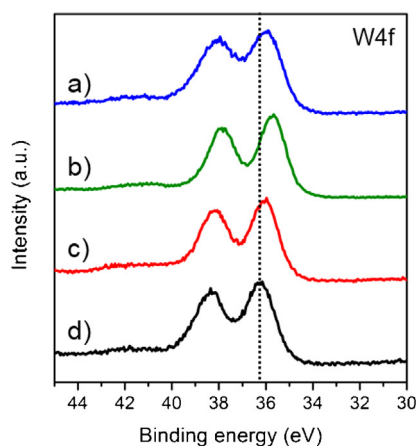

Fig. 6. H_2-TPR profiles of (a) NiW/TMOS-, (b) NiW/TEOS-, (c) NiW/TBOS-silylated Beta(38), and (d) NiW/Beta(38).

Notably, the increment of H_2 consumption in the low temperature range, suggests that metal species supported on silylated Beta(38) get easier to reduce. As the alkyl chain of the used silylation agents was larger, the intensity of the low-temperature peaks grew higher and broader. One conceivable reason is the W and Ni species exposed to the external surface over silylated Beta(38), that enhanced the reducibility [37]. These findings obtained by XPS and TPR analysis indicate the silylated Beta(38) with controlled SiO_2 distribution can alter the electronic properties of metal species, which closely affects the metallic function.

3.4. Acidic properties of silylated Beta zeolites and NiW-supported catalysts

These apparent discrepancy due to the interaction of metal species and supports can be also appeared on acidity in Fig. 7. NH_3-TPD profiles of Beta(38) in Fig. 7a has shown typical two NH_3 desorption peaks observed around 191 °C (weak acidity) and 335 °C

Fig. 5. XPS spectra of W 4f (a-d) and Ni 2p (e-h) for NiW/zeolites: (a, e) NiW/TMOS-silylated Beta(38), (b, f) NiW/TEOS-silylated Beta(38), (c, g) NiW/TBOS-silylated Beta(38), and (d, h) NiW/Beta(38).
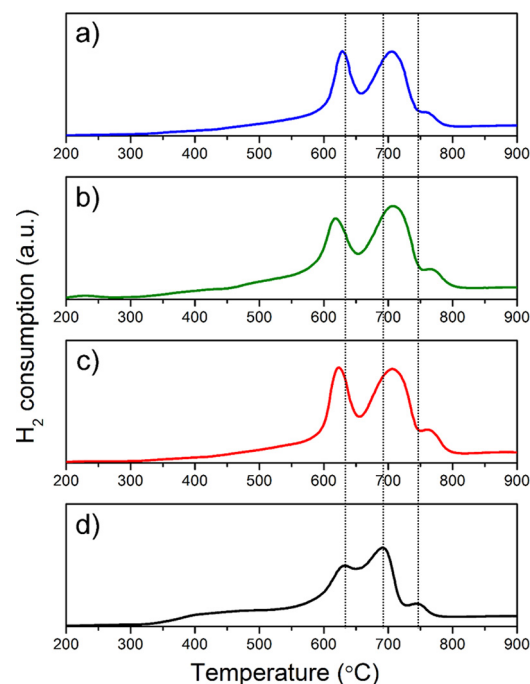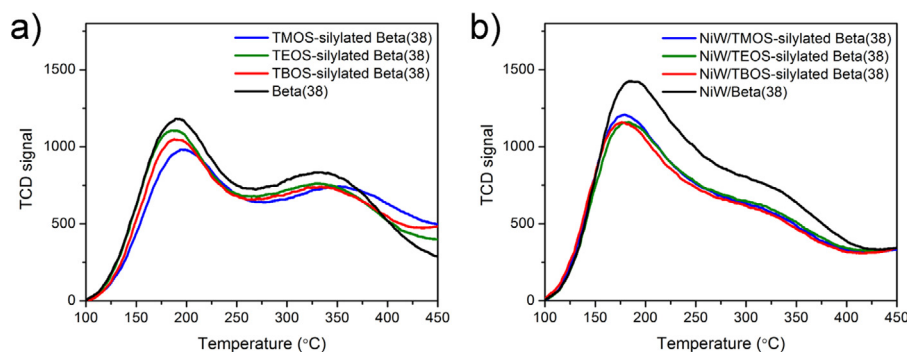
Fig. 7. NH$_3$-TPD profiles of (a) silylated Beta(38) and Beta(38), and (b) NiW/silylated Beta(38) and NiW/Beta(38).
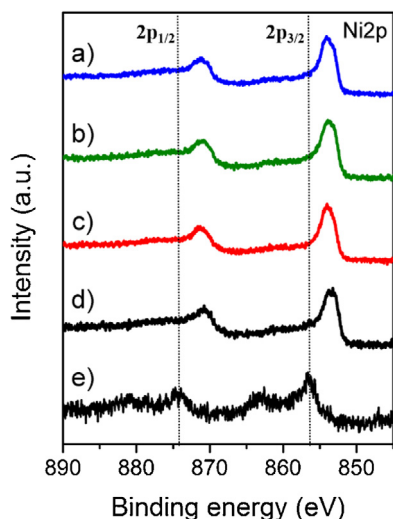

Fig. 8. XPS spectra of Ni 2p for NiW/zeolites with and without sulfidation: (a) NiW/TMOS-, (b) NiW/TEOS-, (c) NiW/TBOS-silylated Beta(38) with sulfidation, and (d) NiW/Beta(38) with sulfidation, and (e) NiW/Beta(38) without sulfidation.
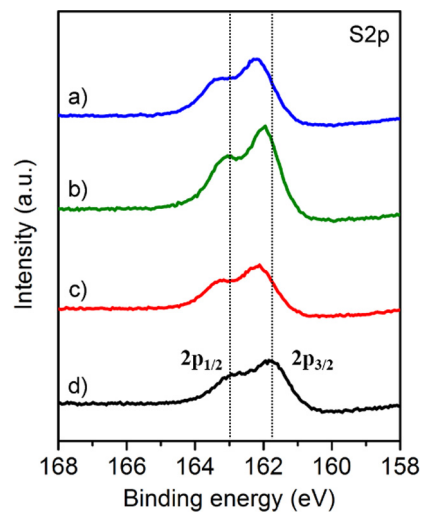

Fig. 9. XPS spectra of S 2p for NiW/zeolites with sulfidation: (a) NiW/TMOS-, (b) NiW/TEOS-, (c) NiW/TBOS-silylated Beta(38) with sulfidation, and (d) NiW/Beta(38) with sulfidation.

(strong acidity). As a result of the passivation of the acid sites on the external surface by the SiO$_2$ layer, all silylated Beta(38) have shown decrease in typical two desorption peaks in correspondence with previously reported literatures [38]. After the impregnation of Ni and W into silylated Beta(38) and bare Beta(38), these two NH$_3$ desorption peaks were preserved at the similar positions, but the peak intensities were changed as seen in Fig. 7b. The amount of ammonia desorbed at lower temperature was higher, because impregnated metal species produced new acid sites through the interaction of the metals and the zeolite acid sites [39]. On the other hand, the amount of desorbed at higher temperature decreased, which seemed that metal species blocked strong acid sites on the surface of the silylated Beta(38) [12,40]. Especially, the NiW/silylated Beta(38) showed more decrease at the higher temperature, which may be relate to the strengthened interaction of metal species and supports confirmed by the XPS result.

3.5. Sulfidation degree of sulfidated NiW/silylated Beta catalysts

Before conducting catalytic performance, all catalysts were sulfidated to alter metal species in the form of metal sulfides. High sulfidation degree may lead to be favorable for getting higher hydrogenation activity, which is expected from metallic function [31]. The formation of metal sulfide was identified by XPS measurement. The Ni 2p spectra of sulfidated samples in Fig. 8 clearly showed peak shift toward lower BE values correlating with Ni in the form of sulfides, so spin-orbit split lines of Ni 2p$_{3/2}$ and 2p$_{1/2}$ were detected at 853.5–853.9 and 870.8–871.2 eV, respectively.

However, the peak positions of Ni supported on silylated Beta(38) remained the same as those supported on the untreated Beta(38). In Fig. 9, the S 2p spectra of all sample after sulfidation treatment showed spin-orbit split lines of S 2p$_{1/2}$ and 2p$_{3/2}$ around 163.0 and 161.8 eV, which is associated mainly with metal sulfide species. However, the observed peak shift would indicate the different sulfidation degree of Ni and W supported on different silylated Beta(38). Specifically, the W 4f spectra of sulfidated NiW/silylated Beta(38) and NiW/Beta(38) were deconvoluted in Fig. 10, and it disclosed that W species were coexisted in the form of WO$_3$ and WS$_2$. Based on the equation of W$_{sulfide}$/W$_{total}$ = W$_{sulfide}$/(W$_{oxide}$ + W$_{sulfide}$), the degree of sulfidation was estimated as described in Table 3 [31]. The result shows that the degree of sulfidation are in the order of NiW/TBOS-silylated Beta(38) > NiW/Beta(38) > NiW/TEOS-silylated Beta(38) > NiW/TMOS-silylated Beta(38). It seems that the silica species in the channel of the silyalted Beta(38) retard the sulfidation of W, but W species over TBOS-silylated Beta(38) maintained the high sulfidation degree because of NiW dominately exposed to the surface. The highest degree of sulfidation in W species implies that it could promote the hydrogenation activity, and thus NiW/silylated Beta(38) is expected to find a favorable sulfidation degree for getting high selective reaction opening reaction.

3.6. Catalytic performance for selective ring opening of 1-methylnaphthalene

To clarify the influence of the SiO$_2$ layer distribution in silylated Beta(38), 1-methylnaphthalene (1-mNap) was chosen as a
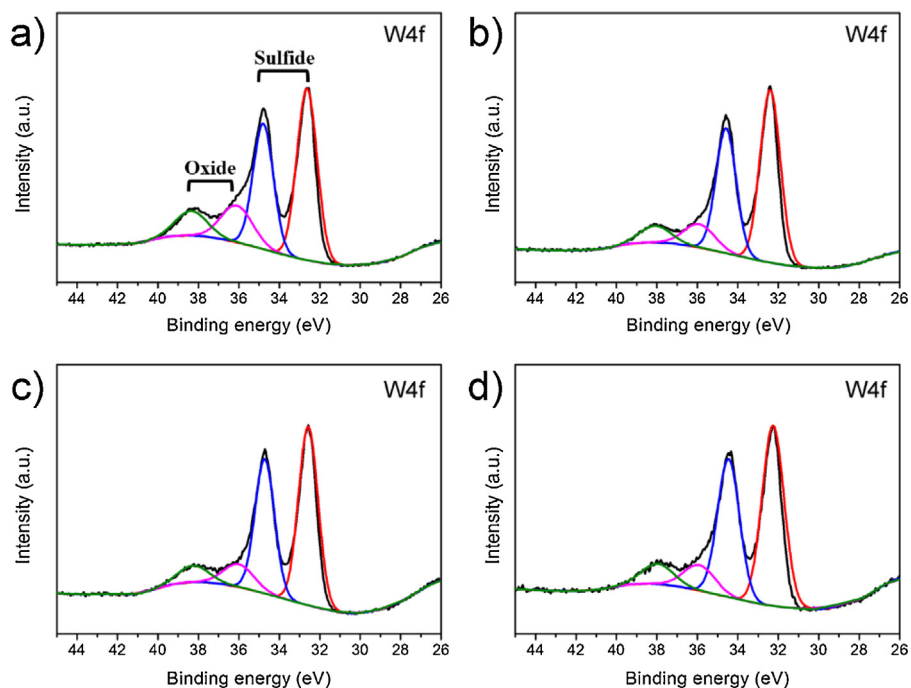
Fig. 10. XPS spectra of W 4f for NiW/zeolites with sulfidation: (a) NiW/TMOS-, (b) NiW/TEOS-, (c) NiW/TBOS-silylated Beta(38) with sulfidation, and (d) NiW/Beta(38) with sulfidation.

Table 3
XPS data of W 4f for NiW/zeolites after sulfidation: peak positions and surface atomic percentages.

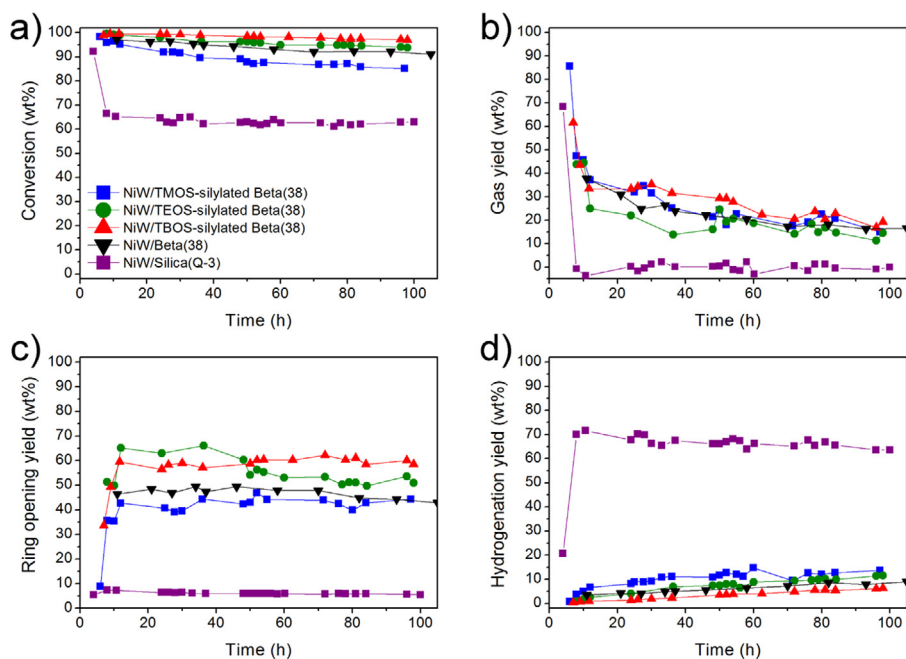| Product	Binding energies (eV)				Atomic percentage (%)	
	WS$_2$		WO$_3$			
	W 4f$_{7/2}$	W 4f$_{5/2}$	W 4f$_{7/2}$	W 4f$_{5/2}$	WS$_2$ (%)	WO$_3$ (%)
NiW/TMOS-silylated Beta(38)	32.6	34.8	36.1	38.3	75.7	24.3
NiW/TEOS-silylated Beta(38)	32.4	34.6	35.9	38.1	83.0	17.0
NiW/TBOS-silylated Beta(38)	32.6	34.7	36.0	38.3	83.7	16.3
NiW/Beta(38)	32.3	34.5	35.9	38.0	83.2	16.8

Fig. 11. Catalytic performance of NiW/silylated Beta(38), NiW/Beta(38) and NiW/Silica(Q-3) catalysts in selective ring opening of 1-mNap over 100 h at 400 °C; (a) conversion, (b) gas yield, (c) ring opening yield, and (d) middle distillate yield.
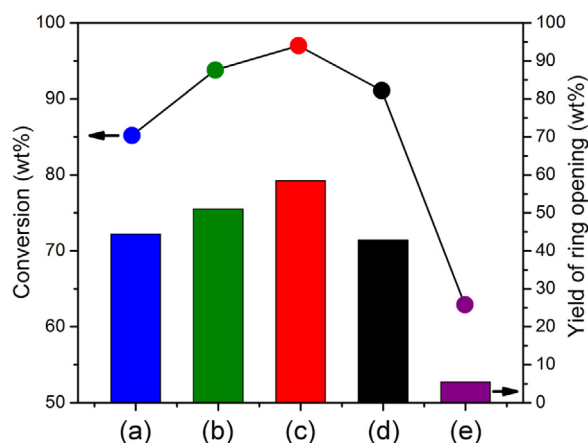
Fig. 12. Conversion and yield of ring opening of (a) NiW/TMOS-, (b) NiW/TEOS-, (c) NiW/TBOS-silylated Beta(38), (d) NiW/Beta(38) and (e) NiW/Silica(Q-3) catalysts in selective ring opening of 1-mNap after 100 h of reaction time at 400 °C.

model compound for the SRO reaction because it is a representative multi-aromatics in heavy oil containing about 45 wt% of di-, tri- and tetra-ring aromatics, usually, with methyl groups [41,42]. More importantly, 1-mNap can easily spread into the channels of silylated Beta(38) zeolite so both external surface and channels participate in the SRO catalytic reaction to take into account the extent of silylation on channels in silylated Beta(38) zeolite. The SRO reaction of 1-mNap was monitored in a typical fixed bed reaction system at 400 °C and 50 bar of hydrogen for 100 h (Fig. 11). Additionally, NiW/Silica(Q-3) were compared under the same condition. Due to that Silica(Q-3) consists of the amorphous silica in the absence of acid sites, the catalytic activity of NiW/Silica(Q-3) can represent the metallic function of NiW supported over SiO_2 layer in NiW/silylated Beta(38). Regarding to the catalytic performance maintained for up to 100 h, the conversion and selective ring opening yield are demonstrated in Fig. 12, and the specific products are summarized in Table S3. Possible products from the SRO reaction of 1-mNap can be proposed to determine the aromatic saturation (hydrogenation) and ring opening (hydrocracking) steps [9,42,43]. The hydrogenation step produces hydrogenation species including tetralin, decalin and alkyl-tetralins, and heavy hydrocarbons meaning multi-ring aromatics heavier than two-ring aromatics. As further ring opening (hydrocracking) step of the hydrogen species proceeds, ring opening species such as alkyl-benzenes including BTEX can be obtained, as the most important target for the SRO reaction. As more cracked products, the light hydrocarbons are cycloalkanes, which are lighter than BTEX, and the most of the gas products consist of alkanes (carbon number 1–4).

In Fig. 11, NiW/Silica(Q-3) exclusively converted 1-mNap into the hydrogenation species with a lower conversion, as a result of the only hydrogenation step from the metallic function. However, to reach ring opening (hydrocracking) products, the ring opening step from the acidic function should be accompanied. In case of NiW/Beta(38) without the silylation, the yield of 42.9 wt% for the ring opening was obtained with the high 1-mNap conversion over 91% after about 100 h of reaction time.

In three cases of NiW/silylated Bata(38), NiW/TEOS-silylated Beta(38) and NiW/TBOS-silylated Beta(38) show the improvement for the 1-mNap conversion and ring opening yield compared with NiW/Beta(38), but NiW/TMOS silylated Beta(38) shows the lowered catalytic performance. It is confirmed from the former characterizations that both NiW/TEOS-silylated Beta(38) and NiW/TBOS-silylated Beta(38) exhibited the silica and NiW metal species more exposed to the external surface [28], the enhanced reducibility [9,38], the high sulfidation degree for WS_2 [22], and

the relatively low acidity. Therefore, the improved catalytic performances of the both catalysts can be estimated due to the strengthened metallic function to force further the hydrogenation activity. As for NiW/TMOS-silylated Beta(38) showed the decreased catalytic performance less than NiW/Beta(38), it may be attributed to the silica and NiW metal species in zeolite channel and the low sulfidation degree for WS_2 despite of the enhanced reducibility.

As the reaction time was prolonged longer than 50 h, NiW/TEOS-silylated Beta(38) has shown a decrease in the ring opening yield. On the reaction time of 100 h (Fig. 11), NiW/TBOS-silylated Beta(38) outperformed NiW/TEOS-silylated Beta(38), maintaining superior conversion (>97.0 wt%) and ring opening yield (>58.5 wt%). Nevertheless, NiW/TEOS-silylated Beta(38) has 93.8 wt% of the conversion and 51.0 wt% of the ring opening yield, still better than those of NiW/Beta(38). To reveal the reason of the deactivation in NiW/TEOS-silylated Beta(38), TGA (Fig. S2) confirmed that the weight loss of spent catalysts indicating the amount of coke formed on catalysts increased in accordance with the catalytic activity. Therefore, the deactivation of NiW/TEOS-silylated Beta(38) could be caused by the coke deposited on the external surface hindered the diffusion into micropores [44,45]. On the other hand, in spite of the highest coke formation, NiW/TBOS-silylated Beta(38) demonstrated the good catalytic stability. It assumed that the hindrance of diffusion into micropores does not affect the bi-functional catalytic activity, due to NiW nanoparticles mainly located at the outer part in NiW/TBOS-silylated Beta(38) (Fig. 3).

Conclusively, NiW/TBOS-silylated Beta(38) has shown the enhanced catalytic performance for the SRO reaction of 1-mNap as a result of the strengthened metallic function confirmed by more exposed NiW particles to the external surface [37], their enhanced reducibility [12,46], and high sulfidation degree for WS_2 [31]. Furthermore, the NiW nanoparticles and SiO_2 layer concentrated on the external surface in NiW/TBOS-silylated Beta(38) can induce that the hydrogenation and hydrocracking steps proceed sequentially like passing through an outer part of NiW/SiO_2 to an inner part of NiW/Beta(38) [14,17,47,48]. The enhancement of the hydrogenation step might efficiently encourage the following hydrocracking step to achieve the high conversion and ring opening yield. Based on these results, it is worth emphasizing that the distribution of SiO_2 layer on the silylated Beta(38) play the key role to alter the balance of metallic and acidic functions, and thus promote the performance of the bi-functional catalyst.

4. Conclusion

In summary, the modification of zeolite was successfully conducted through the silylation reaction by employing TMOS, TEOS, and TBOS. As the size of alkyl chain group in the silylation agents gets larger, the silylation agents were suppressed to spread into the channels and thus the formation of SiO_2 layer was intentionally occurred on the external surface of the zeolite. When NiW metals were supported over each silylated Beta(38) as the bi-functional catalysts, the silylated Beta(38) with different distribution of SiO_2 layer played the key role to determine the distribution of NiW, and thus the NiW nanoparticles were gradually concentrated on the outer part of silylated Beta(38) in the order of NiW/Beta(38) ≈ NiW/TMOS-silylated Beta(38) < NiW/TEOS-silylated Beta(38) < NiW/TBOS-silylated Beta(38). Therefore, three types of NiW/silylated Beta(38) had the different balance of metallic and acidic functions, as confirmed by the metal-support modified electronic structure, reduction activity, sulfidation degree for WS_2, and acidity. Among the various catalysts, NiW/TBOS-silylated Beta(38) showed the best performance toward the SRO of 1-mNap, proving the optimal balance of metallic and acidic functions to encourage the maximum conversion and selective

ring opening yield. We expect that the present strategy will benefit the control over the selective silylation reaction in order to fully harness the modification of the bi-functional catalysts with the optimal balance of metallic and acidic functions, and, hence, to promote properly hydrogenation and ring opening hydrocracking for targeted products.

Acknowledgements

Appendix A. Supplementary data

Supplementary data associated with this article can be found, in the online version, at http://dx.doi.org/10.1016/j.apcatb.2017.07.047.

References

[1] K.X. Lee, J.A. Valla, Appl. Catal. B 201 (2017) 359–369.
[2] Y. Wei, T.E. Parmentier, K.P. de Jong, J. Zecevic, Chem. Soc. Rev. 44 (2015) 7234–7261.
[3] B. Smit, T.L.M. Maesen, Nature 451 (2008) 671–678.
[4] J.-C. Kim, T.-W. Kim, Y. Kim, R. Ryoo, S.-Y. Jeong, C.-U. Kim, Appl. Catal. B 206 (2017) 490–500.
[5] W.E. Farneth, R.J. Gorte, Chem. Rev. 95 (1995) 615–635.
[6] A. Hart, A. Shah, G. Leeke, M. Greaves, J. Wood, Ind. Eng. Chem. Res. 52 (2013) 15394–15406.
[7] G.B. McVicker, M. Daage, M.S. Touvelle, C.W. Hudson, D.P. Klein, W.C. Baird, B.R. Cook, J.G. Chen, S. Hantzer, D.E.W. Vaughan, E.S. Ellis, O.C. Feeley, J. Catal. 210 (2002) 137–148.
[8] M. Santikunaporn, J.E. Herrera, S. Jongpatiwut, D.E. Resasco, W.E. Alvarez, E.L. Sughrue, J. Catal. 228 (2004) 100–113.
[9] E.-S. Kim, Y.-J. Lee, J.-R. Kim, J.-W. Kim, T.-W. Kim, H.-J. Chae, C.-U. Kim, C.-H. Lee, S.-Y. Jeong, J. Nanosci. Nanotechnol. 16 (2016) 1715–1719.
[10] Y. Yang, C. Ochoa-Hernández, V.A. de la Peña O'Shea, P. Pizarro, J.M. Coronado, D.P. Serrano, Appl. Catal. B 145 (2014) 91–100.
[11] Y.-S. Kim, G.-N. Yun, Y.-K. Lee, Catal. Commun. 45 (2014) 133–138.
[12] D. Karthikeyan, N. Lingappan, B. Sivasankar, N.J. Jabarathinam, Ind. Eng. Chem. Res. 47 (2008) 6538–6546.
[13] E.F. Iliopoulou, E. Heracleous, A. Delimitis, A.A. Lappas, Appl. Catal. B 145 (2014) 177–186.
[14] J. Kim, W. Kim, Y. Seo, J.-C. Kim, R. Ryoo, J. Catal. 301 (2013) 187–197.
[15] N. Batalha, L. Pinard, C. Bouchy, E. Guillon, M. Guisnet, J. Catal. 307 (2013) 122–131.
[16] X. Peng, K. Cheng, J. Kang, B. Gu, X. Yu, Q. Zhang, Y. Wang, Angew. Chem. Int. Ed. 54 (2015) 4553–4556.
[17] J. Zecevic, G. Vanbutsele, K.P. de Jong, J.A. Martens, Nature 528 (2015) 245–248.
[18] A.Y. Stakheev, L.M. Kustov, Appl. Catal. A 188 (1999) 3–35.
[19] M.A. Ardagh, Z. Bo, S.L. Nauert, J.M. Notestein, ACS Catal. 6 (2016) 6156–6164.
[20] S. Zheng, H.R. Heydenrych, A. Jentys, J.A. Lercher, J. Phys. Chem. B 106 (2002) 9552–9558.
[21] W.O. Parker, A. de Angelis, C. Flego, R. Millini, C. Perego, S. Zanardi, J. Phys. Chem. C 114 (2010) 8459–8468.
[22] A.B. Halgeri, J. Das, Appl. Catal. A 181 (1999) 347–354.
[23] M.D. Oleksiak, J.A. Soltis, M.T. Conato, R.L. Penn, J.D. Rimer, Chem. Mater. 28 (2016) 4906–4916.
[24] Y. Ji, M.A. Deimund, Y. Bhawe, M.E. Davis, ACS Catal. 5 (2015) 4456–4465.
[25] P. Sharma, M.H. Han, C.-H. Cho, J. Nanomater. 2015 (2015) 1–9.
[26] C.-Y. Lee, G.M. Harbers, D.W. Grainger, L.J. Gamble, D.G. Castner, J. Am. Chem. Soc. 129 (2007) 9429–9438.
[27] A.H. Janssen, A.J. Koster, K.P. de Jong, Angew. Chem. 113 (2001) 1136–1138.
[28] K. Sato, Y. Nisimura, N. Matsubayashi, M. Imamura, H. Shimada, Microporous Mesoporous Mater. 59 (2003) 133–146.
[29] K. Kuroda, A. Shimojima, K. Kawahara, R. Wakabayashi, Y. Tamura, Y. Asakura, M. Kitahara, Chem. Mater. 26 (2014) 211–220.
[30] J.M. Escola, J. Aguado, D.P. Serrano, L. Briones, J.L. Díaz de Tuesta, R. Calvo, E. Fernandez, Energy Fuels 26 (2012) 3187–3195.
[31] G. Wan, A. Duan, Y. Zhang, Z. Zhao, G. Jiang, D. Zhang, Z. Gao, J. Liu, K.H. Chung, Energy Fuels 23 (2009) 3846–3852.
[32] M. Wu, X. Lin, A. Hagfeldt, T. Ma, Chem. Commun. 47 (2011) 4535–4537.
[33] F. Liu, S. Xu, L. Cao, Y. Chi, T. Zhang, D. Xue, J. Phys. Chem. C 111 (2007) 7396–7402.
[34] S. Sabharwal, S. Palit, R.B. Tokas, A.K. Poswal, Bull. Sangeeta, Mater. Sci. 31 (2008) 729–736.
[35] L. Ding, Y. Zheng, Z. Zhang, Z. Ring, J. Chen, J. Catal. 241 (2006) 435–445.
[36] Q. Cui, Y. Zhou, Q. Wei, X. Tao, G. Yu, Y. Wang, J. Yang, Energy Fuels 26 (2012) 4664–4670.
[37] M.H. Jordão, V. Simões, D. Cardoso, Appl. Catal. A 319 (2007) 1–6.
[38] V.V. Ordomsky, J. van der Schaaf, J.C. Schouten, T.A. Nijhuis, J. Catal. 287 (2012) 68–75.
[39] A.M. Alsobaai, R. Zakaria, B.H. Hameed, Chem. Eng. J. 132 (2007) 77–83.
[40] D. Karthikeyan, N. Lingappan, B. Sivasankar, N.J. Jabarathinam, Appl. Catal. A 345 (2008) 18–27.
[41] J.-P. Leininger, F. Lorant, C. Minot, F. Behar, Energy Fuels 20 (2006) 2518–2530.
[42] M.A. Arribas, A. Matinez, Appl. Catal. A 230 (2002) 203–217.
[43] S.G.A. Ferraz, B.M. Snatos, F.M.Z. Zotin, L.R.R. Araujo, J.L. Zotin, Ind. Eng. Chem. Res. 54 (2015) 2646–2656.
[44] K. Kim, T. Lee, Y. Kwon, Y. Seo, J. Song, J.K. Park, H. Lee, J.Y. Park, H. Ihee, S.J. Cho, R. Ryoo, Nature 535 (2016) 131–135.
[45] F. Liu, T. Willhammar, L. Wang, L. Zhu, Q. Sun, X. Meng, W. Carrillo-Cabrera, X. Zou, F.-S. Xiao, J. Am. Chem. Soc. 134 (2012) 4557–4560.
[46] H. Wang, F. Dai, Z. Li, C. Li, Energy Fuels 29 (2015) 4902–4910.
[47] Y. Yamada, C.-K. Tsung, W. Huang, Z. Huo, S.E. Habas, T. Soejima, C.E. Aliaga, G.A. Somorjai, P. Yang, Nat. Chem. 3 (2011) 372–376.
[48] J. Francis, E. Guillon, N. Bats, C. Pichon, A. Corma, L.J. Simon, Appl. Catal. A 409–410 (2011) 140–147.